



Absence of CO₂ electroreduction on copper, gold and silver electrodes without metal cations in solution

Mariana C. O. Monteiro¹, Federico Dattila², Bellenod Hagedoorn¹, Rodrigo García-Muelas², Núria López² and Marc T. M. Koper¹✉

The electrocatalytic reduction of carbon dioxide is widely studied for the sustainable production of fuels and chemicals. Metal ions in the electrolyte influence the reaction performance, although their main role is under discussion. Here we studied CO₂ reduction on gold electrodes through cyclic voltammetry and showed that, without a metal cation, the reaction does not take place in a pure 1 mM H₂SO₄ electrolyte. We further investigated the CO₂ reduction with and without metal cations in solution using scanning electrochemical microscopy in the surface-generation tip-collection mode with a platinum ultramicroelectrode as a CO and H₂ sensor. CO is only produced on gold, silver or copper if a metal cation is added to the electrolyte. Density functional theory simulations confirmed that partially desolvated metal cations stabilize the CO₂⁻ intermediate via a short-range electrostatic interaction, which enables its reduction. Overall, our results redefine the reaction mechanism and provide definitive evidence that positively charged species from the electrolyte are key to stabilize the crucial reaction intermediate.

The electrochemical carbon dioxide reduction reaction (CO₂RR) into fuels and chemicals has recently gained substantial attention as a way to close the chemical carbon cycle and to store excess renewable electricity in fuels and chemicals. Good activity and selectivity of the CO₂RR are crucial to make the process industrially viable. In aqueous media, CO₂ reduction on metals such as gold and silver yields almost exclusively carbon monoxide (in addition to hydrogen from the competing proton and water reduction reactions), whereas on copper C–C bonds are formed¹. Tailoring the catalyst surface is the most common way to steer activity and selectivity. However, it is well-known that the electrolyte composition, especially pH and the cation, has a strong impact on the reaction^{2–4}. To date, in the majority of the studies, alkali metals were employed and the activity trend found on different electrodes is Cs⁺ > K⁺ > Na⁺ > Li⁺ (refs. 5–13). Even though this trend is consistent in different research works, diverging theories have been proposed to explain through which molecular mechanism cations affect CO₂ reduction.

There are three main theories that explain how cations at the interface affect the activity and selectivity of electrocatalytic processes, as recently reviewed by Waagele et al.¹⁴: modification of the local electric field, buffering of the interfacial pH or stabilization of reaction intermediates. On a negatively charged metal electrode, there is still no agreement as to whether cations adsorb specifically, or if their interaction with the surface is purely electrostatic^{15–17}. Especially concerning CO₂RR, Hori and co-workers presented one of the first explanations on how metal cations affect the reaction^{18,19}. Based on Frumkin's theory²⁰, they proposed that cations change the potential profile in the electric double layer through specific adsorption. Weakly hydrated cations lead to steeper potential gradients from the electrode surface towards the outer Helmholtz plane (OHP) compared with those of strongly hydrated species. More recent studies ruled out specific adsorption and instead suggested

that under CO₂RR conditions cations accumulate near the surface via non-covalent interactions to give rise to high electric fields in the vicinity of the ion^{21–23}. For instance, Ringe et al. employed a continuum electrolyte model to show that weakly hydrated cations are more concentrated at the OHP and thus induce a higher mean electronic surface charge density, which in turn leads to an enhanced CO₂RR activity and selectivity²¹. A modification of the potential across the plane on which the electron transfer happens is proposed to change the apparent activation energy of the overall reaction, affect the interfacial water energetics and influence the CO₂ adsorption.

In contrast to the Frumkin-type local electric field effect, a second theory was put forward by Singh et al.²⁴, who proposed that cations affect the CO₂RR by buffering the interfacial pH. Even though alkali cations do not undergo hydrolysis in the bulk, near the negatively charged cathode surface the hydration shell of large cations will experience a stronger electrostatic field, which decreases their pK_a of hydrolysis. Ayemoba and Cuesta²⁵ probed the pH at a gold–electrolyte interface using attenuated total reflection surface-enhanced infrared spectroscopy and based on the ratio between the integrated intensity of the CO₂ and HCO₃⁻ bands, the authors show that larger cations are better buffers and lead to lower pH changes at the interface. Zhang et al.²⁶ performed similar pH measurements using a rotating ring disc electrode and found that during CO₂ reduction in a bicarbonate electrolyte the interfacial pH follows the trend: Li⁺ > Na⁺ > K⁺ > Cs⁺.

The third theory, introduced by Chen et al.²² and further developed in the work of Resasco et al.²⁷, suggests that metal cations stabilize certain CO₂RR intermediates through local electrostatic interactions within the electrical double layer. Specifically, the study of Resasco et al.²⁷ focused on the effect of alkali cations on CO₂ reduction over Cu(100) and Cu(111) thin-film electrodes and Ag and Sn polycrystalline electrodes. The formation of CO was

¹Leiden Institute of Chemistry, Leiden University, Leiden, the Netherlands. ²Institute of Chemical Research of Catalonia (ICIQ), The Barcelona Institute of Science and Technology (BIST), Tarragona, Spain. ✉e-mail: m.koper@lic.leidenuniv.nl

suggested to happen through the reaction intermediates shown in equations (1)–(3), where the gold surface site is represented by an asterisk (*):



The selectivity trends reported in Resasco et al.²⁷ are explained through density functional theory (DFT) simulations on a surface/solvated cation interface optimized via constrained minima hopping molecular dynamics. Solvated cations with a larger ionic radius experience a stronger driving force and accumulate near the surface²⁷. As previously demonstrated by Chen et al.²², high local electrostatic fields generated by solvated cations can locally stabilize adsorbed intermediates with large dipole moments. Thus, the higher activity observed for CO₂ reduction on copper in the presence of larger cations was attributed to a higher concentration of such cations in the OHP²⁷.

To test the above models, we carried out CO₂ reduction experiments on polycrystalline gold, which is a stable and simple electrocatalytic system that, under the conditions of this study, yields only CO and H₂. Measurements were performed in the total absence of metal cations (at pH=3) and in the presence of small amounts of Cs⁺. Using scanning electrochemical microscopy (SECM) in the surface-generation tip-collection mode as an extremely sensitive technique to detect CO₂ reduction products, we showed that without a metal cation in solution, CO₂ reduction does not take place. This remarkable observation was extended to other common catalysts, such as copper and silver. Of the three models described in the literature, only the model that considers electrostatic interactions between metal cations and key intermediates can explain this observation. We further confirmed the role of cations through ab initio molecular dynamics (AIMD) simulations on a gold/cation/solvent system in which we proved the stabilization effect of partially desolvated metal cations on CO₂ adsorption, activation and formation of the CO₂⁻ intermediate. Although our results, in principle, do not exclude contributions from the other two models, they nonetheless clearly show that the main role of the metal cation is to stabilize the key CO₂⁻ intermediate, to the extent that in its absence, CO₂ reduction does not take place. This conclusion has important implications for CO₂RR modelling and catalyst design.

Results

Hanging meniscus experiments. To elucidate the role of metal cations in the CO₂RR, the reaction was first studied through cyclic voltammetry (CV) using a gold electrode in a hanging meniscus configuration. On gold, under the conditions of this study, CO₂ is reduced in the cathodic scan to produce only CO. The competing hydrogen evolution reaction occurs due to the reduction of protons or water, depending on the interfacial proton concentration. As gold is also a very good catalyst for CO oxidation (CO_{ox}), the CO produced can be probed semiquantitatively by directly cycling the electrode to positive potentials. The gold electrode used in this study was characterized by blank voltammetry before each measurement (Supplementary Discussion and Supplementary Fig. 1) to assure the cleanliness of the surface, and the comparability and reproducibility of the experiments, and to allow the determination of the electrochemically active surface area. This consecutive cathodic/anodic cycling was performed first in argon and subsequently in a CO₂ atmosphere. Figure 1a compares the cathodic scans obtained in the absence of a metal cation (in 1 mM H₂SO₄)

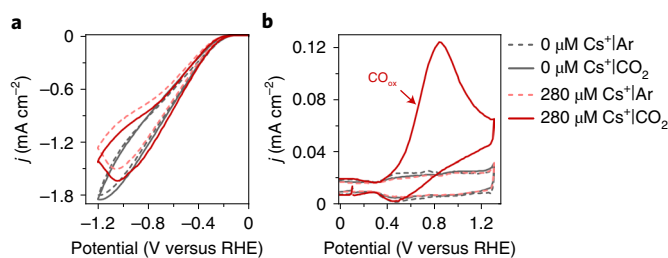


Fig. 1 | CO₂ reduction on gold with and without 280 μM Cs⁺ in solution. **a, b,** Cathodic scans recorded in argon and CO₂ atmosphere (**a**) and the subsequent recorded anodic scans performed to oxidize any CO produced (**b**). All the CVs were recorded at 50 mV s⁻¹.

and in the presence of 280 μM of Cs⁺, both solutions at bulk pH=3. Note that an experiment in the absence of metal cations (which is the focus of this work) can only be performed at this or at a lower pH, as for a higher pH without metal cations the electrolyte conductivity becomes prohibitively small. Still, owing to the local production and consumption of OH⁻ and H⁺, respectively, the alkalinity at the interface increases during the course of the reaction. In argon, when only hydrogen evolution takes place, the proton reduction current is lower and reaches diffusion limitation at lower overpotentials than in the presence of Cs⁺. This is probably due to migration, which with Cs⁺ in solution leads to a lower concentration of protons near the surface. This is further confirmed by the fact that when we increased the Cs⁺ concentration (at pH=3), the proton reduction current was even lower (Supplementary Discussion and Supplementary Fig. 2). In a CO₂ atmosphere, the reduction current increased more substantially in the presence of 280 μM Cs⁺, whereas almost no increase was observed in pure H₂SO₄. In Fig. 1b, we show that in the absence of Cs⁺ no CO was detected in the anodic scan and the only current observed is due to charging of the electrical double layer, which nearly overlaps for both gaseous atmospheres. With Cs⁺ in the electrolyte a large anodic current due to the oxidation of the CO produced was observed. Unlike CO₂ reduction, CO_{ox} did take place in the absence of a metal ion in the electrolyte, as seen in the control experiment (Supplementary Discussion and Supplementary Fig. 3). To further confirm that Cs⁺ is crucial for enabling the CO₂RR, which causes the CO_{ox} current observed, we gradually added different amounts of Cs⁺ ions to the electrolyte (Supplementary Discussion and Supplementary Fig. 4). The amount of CO produced increased as a function of the Cs⁺ concentration in the electrolyte, as derived from the CO_{ox} currents from the CVs. Three subsequent CVs were recorded for every concentration and the trend remains the same over the different cycles.

This enhancement in the CO production with the addition of Cs⁺ ions was investigated in a broader concentration range using Li₂SO₄ as the background electrolyte at pH=3. Here the total cation concentration was kept constant (0.1 M) to avoid contributions from solutions of different ionic strengths. The gold electrode was cycled from 0 to -1 V versus the reversible hydrogen electrode (RHE) in the different electrolytes and the CO produced was oxidized in the positive-going scan, similarly to previous experiments (Fig. 1). The CV is presented in Supplementary Fig. 5 and the charge of the CO_{ox} peak found for the different concentrations of Cs⁺ is depicted in Fig. 2. With the addition of less than 1 mM Cs⁺ to the electrolyte, a steep increase in the CO production is observed. At higher concentrations, a saturation effect appears as the CO production approximates to a plateau.

We also used the cathodic/anodic voltammetry during CO₂ reduction on gold to evaluate different metal cations in the dilute electrolytes used in this work. The gold electrode was flame annealed and characterized before each measurement and the blank

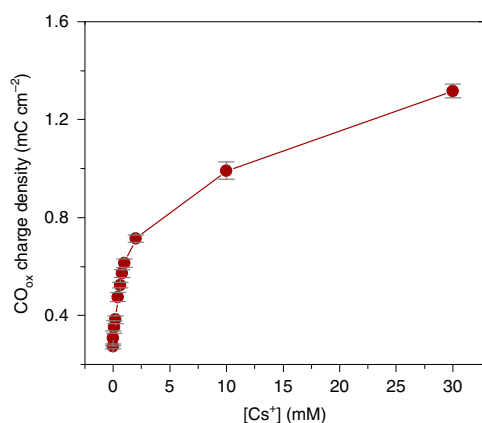


Fig. 2 | Effect of the Cs⁺ concentration. CO produced after polarization to -1V versus RHE in the presence of different concentrations of Cs⁺ in a Li₂SO₄ background electrolyte. The total cation concentration in solution was kept at 0.1M and the pH=3. Error bars (s.d.) are calculated based on three individual measurements.

voltammograms can be seen in Supplementary Fig. 1. Experiments were performed in 1 mM M₂SO₄, where M=H, Li, Na, K or Cs. All the solutions, if necessary, were adjusted to pH=3 to exclude pH effects. Figure 3 shows the CO_{ox} charge of the first anodic cycle recorded after performing CO₂ reduction from 0 to -1.2V versus RHE. The activity for CO formation correlates with the size of the solvated cation, here represented by the cation–oxygen (M⁺–H₂O) bond length. The bond length for each alkali metal was taken as the first peak of the cation–water radial distribution functions obtained from AIMD data (Supplementary Methods and Supplementary Table 1), and for the cation-free electrolyte, the proton–oxygen (H⁺–H₂O) bond length was used²⁸. In agreement with the previous results, no CO₂ reduction product was observed in the absence of a metal cation, but in the M₂SO₄ electrolytes the activity for CO production followed the usual trend reported for other metal surfaces: Cs⁺ > K⁺ > Na⁺ > Li⁺ (ref. 3). We observed a strong correlation between activity and the cation size, which is related to a softer hydration shell, and thus favours the production of CO (see computational model discussion).

Scanning electrochemical microscopy. To confirm that in the absence of a metal cation absolutely no CO is produced on gold and to extend the study to silver and copper, relevant CO₂RR catalysts which are not good for CO_{ox}, we employed SECM in the surface-generation tip-collection mode to detect CO₂ reduction to give CO. A schematic representation of the experiments is shown in Fig. 4a. A platinum ultramicroelectrode (Pt-UME) was placed in the diffusion layer above the substrate electrode at which CO₂ reduction takes place. Platinum voltammetry is extremely sensitive to trace amounts of CO, as CO strongly chemisorbs on the surface and can be removed by oxidation²⁹. Platinum is also a suitable catalyst for hydrogen oxidation, and thus we can also detect hydrogen produced due to the hydrogen evolution reaction. SECM was used here because of the higher sensitivity that it provides to detect CO in comparison with other product analysis techniques, such as gas chromatography and differential electrochemical mass spectrometry. The procedure used for all the measurements is shown in Fig. 4b. A negative potential was applied to the sample for ten seconds and subsequently a cyclic voltammogram of the Pt-UME was recorded. Special care was taken with the samples and electrolytes used in these experiments to make sure traces of metal impurities would not mislead our conclusions. The Pt-UME was prepared and characterized before each measurement. A blank voltammogram

of the Pt-UME can be seen in Fig. 4c, which shows the expected voltammetric features of a clean polycrystalline platinum surface³⁰. The polycrystalline gold, copper and silver samples used were also characterized before the measurements, as shown in Fig. 4d–f, respectively. The voltammetry of copper and silver electrodes used for CO₂RR studies is rarely shown in the literature, despite its importance to determine the quality of the surface preparation and consequently reproducibility of the experiments. Here silver was characterized through the reversible Tl(I) underpotential deposition, which is used to assess the surface cleanliness and crystallinity³¹. This is seen by the presence and reversibility of the peaks from Fig. 4e. To evaluate the copper sample, the electrode was characterized in concentrated hydroxide solution, and the current due to the adsorption and desorption of OH⁻ can be observed in the region of Cu₂O formation, which also indicates the surface crystallinity³².

The SECM measurements were carried out in 1 mM H₂SO₄ with and without the addition of 280 μM Cs⁺. For each electrolyte, before the CO₂ reduction, a control experiment in argon was performed, with only hydrogen expected as a product. The Pt-UME was always positioned $50 \pm 2\ \mu\text{m}$ from the surface by performing a capacitive approach in air, which is essential to keep the electrolyte free from impurities^{33–35}. The uncertainty in the position is the error from the approach curve fits. Approach curves and details on the curve fitting are reported in Supplementary Fig. 6 (Supplementary Discussion and Supplementary equation (1)). Figure 5a shows the results obtained for the gold electrode after applying a potential of -0.7V versus RHE to the sample. In an argon atmosphere, in the absence or presence of Cs⁺, only a current characteristic of hydrogen oxidation was seen in the Pt-UME voltammetry. In a CO₂ atmosphere, and only when Cs⁺ was added to the electrolyte, a sharp peak due to the oxidation of CO occurred, which confirms that CO₂ reduction on gold does not take place in the absence of a metal cation in solution. Figure 5b shows similar results for the silver electrode at a potential of -0.8V versus RHE. As for gold, on silver CO₂ reduction took place only in the Cs⁺-containing electrolyte, as confirmed by the CO_{ox} peak in the Pt-UME voltammetry. On copper, the same trend was observed when the sample was polarized at -1V versus RHE (Fig. 5c). In the 1 mM H₂SO₄ electrolyte only hydrogen was detected by the Pt-UME, whereas CO was detected only after the addition of Cs⁺ to the electrolyte. It must be noted that these

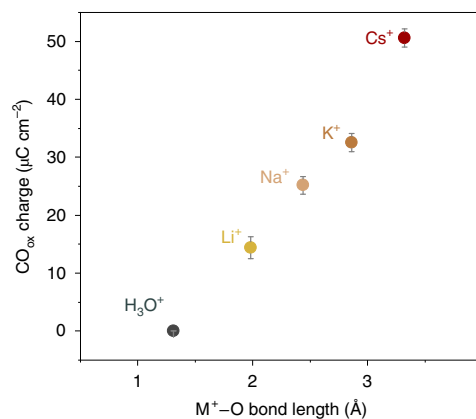


Fig. 3 | Effect of the cation identity. CO detected on the gold sample directly after CO₂ reduction from 0 to -1.2V versus RHE in 1 mM M₂SO₄ with M=H, Li, Na, K or Cs. All the solutions, when necessary, were adjusted to pH=3. The M⁺–O bond length is taken as the first peak of the cation–water radial distribution functions obtained from AIMD data (Supplementary Table 1), but in the absence of a metal cation we used the proton–oxygen bond length²⁸. Error bars (s.d.) are calculated based on three individual measurements.

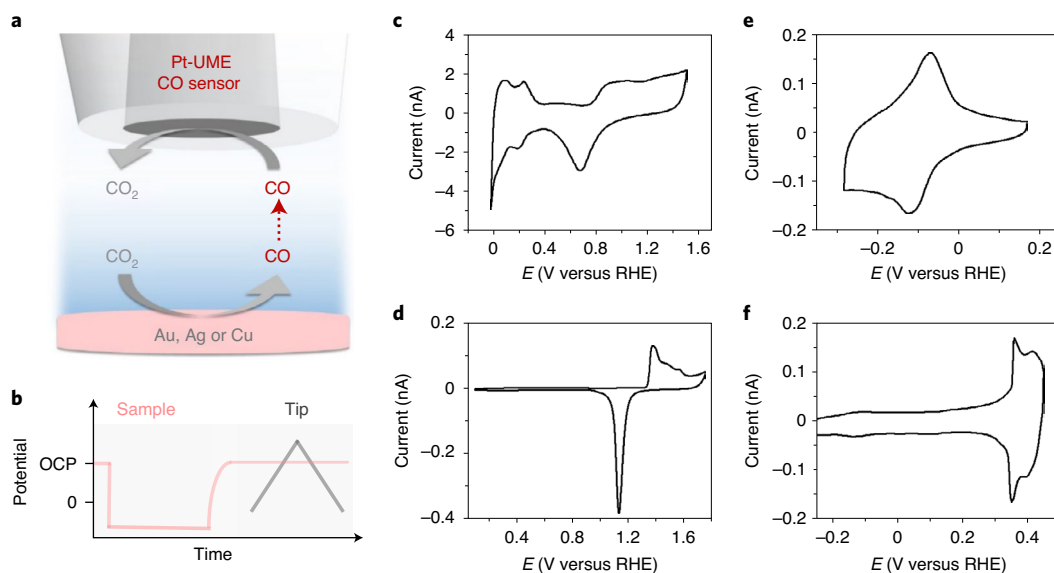


Fig. 4 | SECM measurement scheme and characterization of the electrodes used. **a, b**, Schematic representation of the SECM experiment (**a**) and method used to perform the measurements (**b**). **c**, Blank voltammetry of the Pt-UME used to perform the experiments taken in 0.1 M H₂SO₄. **d–f**, Characterization of the gold sample in 0.1 M H₂SO₄ (**d**), the silver sample through TI(1) under potential deposition in 0.5 M Na₂SO₄ + 0.1 M H₂SO₄ + 0.1 M Ti₂SO₄ (**e**) and the copper sample in 0.5 M NaOH (**f**). All the sample characterization CVs were recorded at 50 mV s⁻¹.

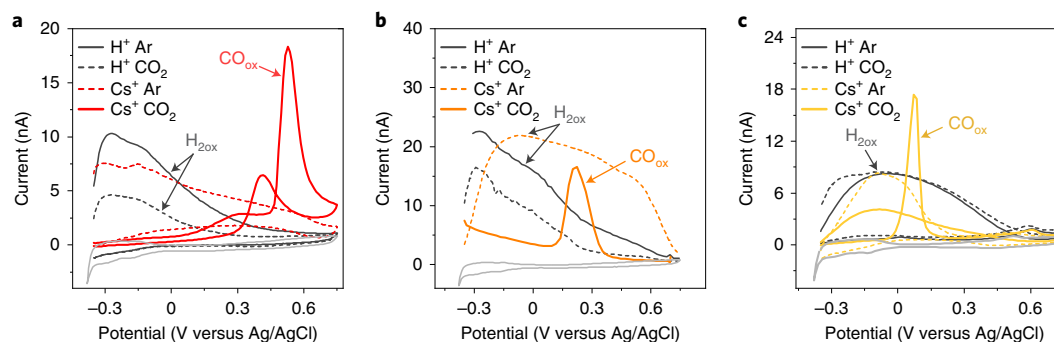


Fig. 5 | CO detection with SECM. **a–c**, CV of the Pt-UME taken directly after CO₂ reduction on gold (**a**), silver (**b**) and copper (**c**) electrodes. The voltammetry of the Pt-UME before applying any potential to the sample is shown in light grey for reference.

individual SECM measurements constitute only a qualitative tool to probe whether CO was formed or not. Owing to various factors, such as the different sample potentials applied, bubble formation and diffusion hindrance by the tip, the magnitude of the CO and H₂ oxidation currents measured and their potentials cannot be used for a quantitative comparison between the substrates. For silver and copper, the potential range applicable was limited by the stability of the electrode. At more cathodic potentials, a small amount of metal oxide dissolution was observed and the traces of Ag⁺ and Cu²⁺ ions released into the electrolyte led to the production of CO in 1 mM H₂SO₄ (Supplementary Discussion and Supplementary Fig. 7)³⁶. This happens as during the SECM approach, the electrode surface is exposed to air, which can lead to the formation of (a very small amount) of oxide on the surface. This was confirmed by the Pt-UME voltammetry (Supplementary Fig. 7), which presented voltammetric features characteristic of the underpotential deposition of Ag⁺ or Cu²⁺ on the Pt-UME surface^{37,38}.

Computational model. To model the experimental system via density functional theory (DFT), we carried out AIMD on a (3√3 × 3√3)

R30° Au(111) supercell (four layers, 15.3 Å × 15.3 Å × 30.0 Å) with 72 explicit water molecules filling 15.0 Å along *z*, plus an 8 Å vacuum thickness between periodic slabs (Supplementary Methods, Supplementary Fig. 8 and Supplementary Videos 1–5)³⁹. This pristine system (Au–H₂O) was equilibrated for 2 ps at 300 K with a time step of 1 fs, as illustrated in Fig. 6a. Then, an alkali metal cation M⁺ (M = Li, Na, K or Cs) was inserted close to the gold surface, at an initial cation–surface distance of 3.3 Å. On optimization, the cation–surface distances increased for each alkali metal (Supplementary Fig. 9). To specifically investigate the local interactions between cation and CO₂, we kept the cation concentration at the OHP constant—to balance the charge within the unit cell we included an OH⁻ at the fourth water bilayer (Methods). Given the volume of the solvation layer and the number of water molecules, the cation surface coverage (0.04 monolayers (ML)) corresponds to a molar concentration of around 0.5–0.8 M (Supplementary Methods). As the initial position and surface coverage were identical for each cation, concentration effects were not included in the model. We let the cation solvation shell build up for 2 ps and classified the final structures as Au–H₂O–M⁺ (Fig. 6a and Supplementary Fig. 8). The resulting cation–oxygen

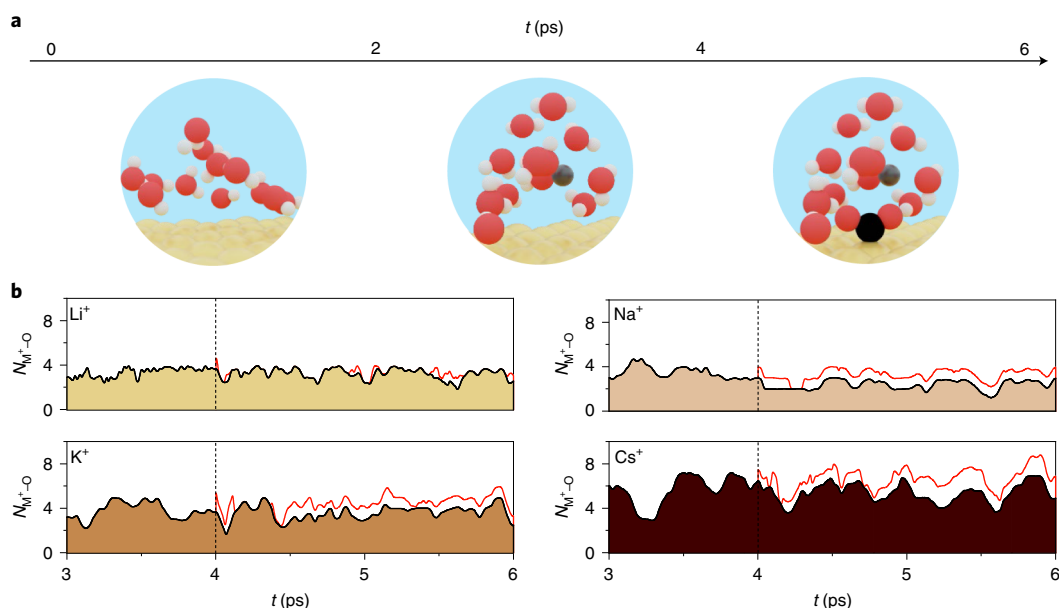


Fig. 6 | Cation coordination with CO₂. **a**, Timeline for the AIMD simulation at 300K: 2 ps pre-equilibration for the Au-H₂O system, 2 ps for the Au-H₂O-M⁺ system (cation inserted close to the surface, $\theta_{M^+} = 0.04$ ML) and finally 2 ps for the Au-H₂O-M⁺-CO₂ system (CO₂ molecule adsorbed on Au). The portrayed cation is Li⁺. **b**, Alkali cation's coordination number, N_{M^+-O} , versus simulation time for the Au-H₂O-M⁺ system. Dashed lines indicate CO₂ insertion into the supercell ($t = 4$ ps) and red lines indicate the increase in coordination number due to M⁺-O(CO₂).

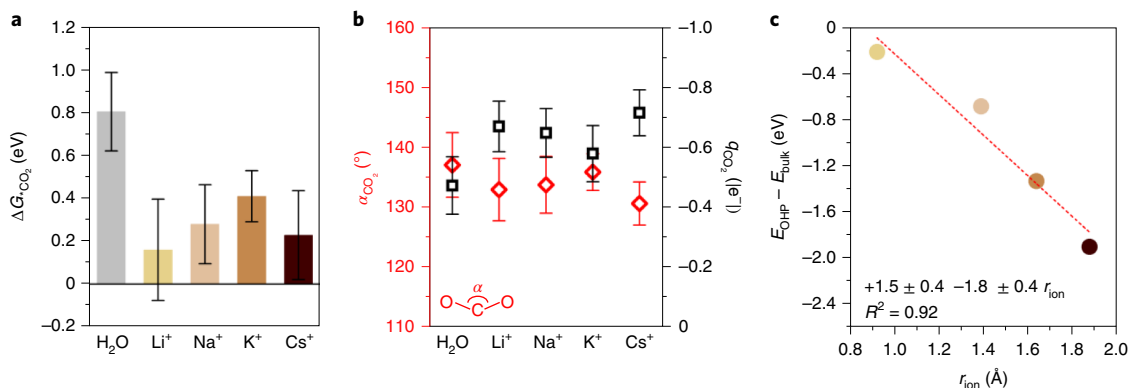


Fig. 7 | CO₂ activation via an explicit cation-intermediate interaction, driven by cation concentration at the OHP. **a**, Average CO₂ adsorption Gibbs free energy at $U = 0$ V versus standard hydrogen electrode (SHE) in the absence (grey) or presence (light to dark brown) of an alkali cation, with CO₂ and the environment (Au-H₂O or Au-H₂O-M⁺) as the energy references. **b**, α_{CO_2} and CO₂ Bader charge, q_{CO_2} , are shown in red and black, respectively, and reported in Supplementary Table 4. Error bars are calculated as the s.d. of the data (Methods). **c**, Correlation between thermodynamic driving force at $U = 0$ V versus SHE for different alkali cations that accumulate at the OHP and their ionic radius (Methods).

radial distribution functions $g_{M^+-H_2O}(r)$ (Supplementary Methods, Supplementary equations (2) and (3) and Supplementary Fig. 10) confirmed a proper description of the cation coordination shell, as the estimated cation-oxygen distances d_{M^+-O} for water molecules in the first solvation shell agreed with previous experimental and theoretical results (Supplementary Table 1). Furthermore, the full width at half maximum for the first $g_{M^+-H_2O}(r)$ peak increased according to the alkali group $Li^+ < Na^+ < K^+ < Cs^+$, which thus confirms that a larger cation ionic radius implies a softer solvation shell. Finally, we estimated the cation coordination numbers through the structural parameters previously defined (Supplementary Methods and Supplementary equations (4) and (5)). The alkali cations exhibited an average coordination number of 2.8, 3.2, 3.5 and 5.8 with maximum values of 3.9, 4.7, 4.9 and 8.0 for Li⁺, Na⁺, K⁺ and Cs⁺,

respectively (Supplementary Table 2), in line with state-of-the-art reported values⁴⁰.

After the equilibration of the Au-H₂O-M⁺ systems, we introduced a CO₂ molecule at the electrolyte/surface interface in the proximity of the solvated cation (Supplementary Figs. 6a and 8). On AIMD simulations for an additional 2 ps, CO₂ adsorbed on the gold surface in a η^2_{CO} conformation (bidentate through the carbon atom and one oxygen) and coordinated to the surrounding cation and water molecules through the second oxygen. Owing to its hard solvation shell, Li⁺ coordinates to CO₂ for limited periods of the AIMD runs, which resulted in an average coordination number $N_{Li^+-O(CO_2)}$ of 0.1 ± 0.3 (Fig. 6b, Supplementary Table 2). Instead, other alkali metals continuously bind to the oxygen atom in CO₂, here called O(CO₂), which resulted in the following

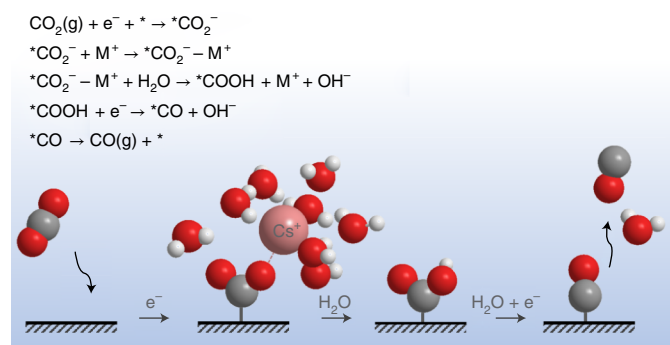


Fig. 8 | Mechanism of CO₂ reduction to CO. Schematic representation of the interaction of the cation with the negatively charged CO₂⁻ intermediate together with a proposed reaction mechanism.

coordination numbers: $N_{\text{Na}^+ - \text{O}(\text{CO}_2)} = 0.9 \pm 0.2$, $N_{\text{K}^+ - \text{O}(\text{CO}_2)} = 0.9 \pm 0.4$ and $N_{\text{Cs}^+ - \text{O}(\text{CO}_2)} = 1.3 \pm 0.5$. On coordination to $\text{M}^+ - \text{O}(\text{CO}_2)$, the number of water molecules within the cation's coordination shell remained constant or slightly decreased (Fig. 6b and Supplementary Table 2).

Partially desolvated cations have three promotional effects which enable CO₂ reduction. The first effect is thermodynamic (Fig. 7a). When the cation coordinates to the adsorbate, a short-range $\text{M}^+ - \text{O}(\text{CO}_2)$ electrostatic interaction stabilizes CO₂ more strongly than the solvation by water molecules alone by around 0.5 eV (Fig. 7a, equation (4) and Supplementary Table 3). Besides, there is a medium-range interaction between the electric dipole of adsorbed $* \text{CO}_2^-$ and a cation-induced electric field, which is irregular and modulated by the electrolyte, solvation and neighbouring cations (Supplementary Note 1, Supplementary equations (6) and (7) and Supplementary Fig. 11)^{22,27,41}. Both short- and medium-range cation-induced interactions account for an equivalent stabilizing effect. Instead, in the absence of cations, the medium-range $* \text{CO}_2^-$ -dipole/electric field interaction only accounts for a weaker stabilization (-0.2 eV), unable to open the CO₂ reduction pathway (Supplementary Note 2, Supplementary equation (8) and Supplementary Fig. 12). The second promotional effect can be observed in the O-C-O angle α , α_{CO_2} , which decreases from linear 180° to below 140° in the presence of a neighbouring cation, indicating the activation of CO₂ (Fig. 7b, red axis, and Supplementary Table 4). Third, on coordination, cations enhance the electron transfer from the catalytic surface to the CO₂ unit, as demonstrated by the CO₂ Bader charges close to -1.0|e⁻| (Fig. 7c and Supplementary Table 4). Thus, partially desolvated cations are crucial for the formation of the CO₂⁻ intermediate, the generally assumed rate-determining step for CO₂ reduction⁴². As a final remark, the activity trends based solely on cation radius (Fig. 3) originate both from different cation surface concentrations at the OHP (Fig. 7c and equations (5)–(8))²⁷ and their different ability to coordinate to $* \text{CO}_2^-$, which ranges from almost no bond for Li⁺ to more than a bond for Cs⁺ (Supplementary Table 2).

Discussion

The results presented here show that without a metal cation in the electrolyte, CO₂ reduction to CO does not take place on gold, silver and copper electrodes. As discussed earlier, there are currently three major theories as to the main role of metal cations during CO₂ reduction: modification of the (local) electric field, buffering of the interfacial pH and stabilization of the reaction intermediates via local field effects. All the theories have been supported with experiments and DFT models, and to some extent they all play a role on the CO₂RR. However, based on our experimental and theoretical results, we rule out that the modification of the local electric field or

buffering of the local pH are the main reasons for the cation effects observed. These theories suggest that the cation should just affect the CO₂ reduction rate and that this reaction should still take place in cation-free electrolytes. Our results also confirm the view suggested by Chen et al.²² and Resasco et al.²⁷, that a key role of cations on CO₂ reduction is to stabilize negatively charged reaction intermediates, such as $* \text{CO}_2^-$ (and $* \text{OCCO}^-$) via a local electric field effect. Besides the medium-range electric field–electric dipole interaction, we show here that an explicit short-range local electrostatic interaction between a partially desolvated metal cation and CO₂ accounts for a similar stabilization. Figure 8 shows our proposed reaction mechanism based on the discussed experimental and computational results, together with a pictorial representation. Here we suggest that the cation is the crucial promoter to enable the reduction process as it forms a complex with CO₂, which allows the formation of the CO₂⁻ intermediate. Additionally, as shown in Fig. 1b, the more Cs⁺ added to the electrolyte, the more CO produced, similarly to ethylene formation on copper, which follows the cation radius trend $\text{Cs}^+ > \text{K}^+ > \text{Na}^+$ (ref. 27). Here we propose that the differences in activity observed among the alkali cations for CO₂ reduction correlate with their different concentrations at the OHP (Fig. 7c) and their different capability of interacting with negatively charged adsorbates, as indicated by the substantially different cation–CO₂ average coordination numbers over the 2 ps simulation time (Fig. 6b and Supplementary Table 2). Metal cations with a softer hydration shell have a higher concentration at the interface and show a stable coordination with CO₂ (Na⁺, K⁺ and Cs⁺; Fig. 6b), and thus they are more likely to stabilize it via a $\text{M}^+ - \text{O}(\text{CO}_2)$ local interaction. Instead, hard shell cations, such as Li⁺, coordinate poorly with CO₂ and thus enable this stabilization effect less effectively.

The knowledge that CO₂ can only be reduced in the presence of a metal cation interacting with the CO₂⁻ intermediate has important implications. From the system-design point-of-view, research efforts should focus on finding species that might have an even larger stabilizing effect on CO₂ than that of Cs⁺, such as large multivalent cations⁴³ or surfactants⁷. Additionally, from the reaction modelling point-of-view, our results highlight that an accurate understanding of the electrochemical activation of CO₂ on copper, silver and gold must involve cations and water. To simply assume a proton-coupled electron transfer as a first step in DFT-based electrocatalysis fails to account for the stabilization of the key reaction intermediates by electrolyte cations^{44–46}. Instead, we here show that the explicit inclusion of cationic species allows the stabilization of the CO₂⁻ intermediate by around 0.5 eV and is needed to properly estimate its energy. Finally, our mechanism suggests that, at least for a pH of 3 or higher, water is the relevant hydrogen/proton donor, rather than hydronium itself, which cannot activate CO₂. As a result, the CO₂RR does not consume protons, but it generates OH⁻. This statement agrees with, and provides an explanation for, our recent observation that in mildly acidic media, CO₂ reduction can completely suppress the proton reduction to hydrogen by neutralizing protons through the generated OH⁻, which renders the protons no longer available for hydrogen formation⁴⁷.

Methods

CV experiments. CO₂ reduction measurements were performed in a three-electrode glass cell in which the reference was a RHE, separated from the work compartment by a Luggin capillary, and the counter electrode was a gold wire (0.8 mm thick, Mateck, 99.9%). Polycrystalline gold (0.5 mm thick, MaTecK, 99.995%) discs 5 mm in diameter were used as the working electrode in the hanging meniscus configuration. The surface was first prepared by grinding with a silicon carbide paper (grit size 600, MaTecK) and then by polishing on a microcloth (Buehler) with different diamond suspensions (MetaDi 3, 1, 0.25 and 0.05 μm, Buehler) for 2 min for each size. The electrodes were immersed in ultrapure water (>18.2 MΩ cm, Millipore Milli-Q) and cleaned in an ultrasonic bath (Bandelin SONOREX RK 52 H) for 3 min between polishing steps. Between the experiments, the electrode was flame annealed using a butane torch following the procedure previously reported⁴⁸. After each flame annealing, the

electrode was characterized by CV in 0.1 M H₂SO₄ (Merck, Suprapur, 96%). The electrochemical surface area was determined using the charge that corresponded to the gold oxide reduction peak. The charge was converted into surface area using the charge density associated with the reduction of a monolayer of gold oxide (386 μC cm⁻²) (ref. 49). Prior to the experiments, the glassware was stored in potassium permanganate solution (1 g l⁻¹ KMnO₄ dissolved in 0.5 M H₂SO₄), and afterwards cleaned by immersion in dilute piranha and boiled at least five times in ultrapure water. Measurements were performed in 50 ml of the electrolyte using a Bio-Logic potentiostat/galvanostat/EIS (SP-300). The experiments in the absence of metal cations were performed in 1 mM H₂SO₄ (Merck, Suprapur, 96%). Other measurements were performed using different high-purity sulfate electrolytes: 1 mM Li₂SO₄ (Alfa Aesar, anhydrous, 99.99%, metals basis), 1 mM Na₂SO₄ (Alfa Aesar, Puratronic, 99.9955%, metals basis), 1 mM K₂SO₄ (Alfa Aesar, Puratronic, 99.997%, metals basis) and 1 mM Cs₂SO₄ (Alfa Aesar, Puratronic, 99.997%, metals basis). During the measurements the electrolyte was constantly purged with argon or CO₂ and the pH was always adjusted to 3 using H₂SO₄. The solution resistance was determined by potentiometric electrochemical impedance spectroscopy prior to every measurement and the electrode potential was always automatically compensated for 85% of the ohmic drop.

SECM measurements. The SECM measurements were performed in our home-built SECM set-up, previously described elsewhere³³. The SECM cell cleaning method and all the equipment used are the same as those previously reported³³. The SECM samples were prepared and characterized prior to every measurement. The polycrystalline gold, silver and copper samples were mechanically polished exactly as described for the gold disc used in the hanging meniscus experiments. The copper sample was further electropolished in 66% H₃PO₄ at 3 V versus a Cu counter electrode for 10 s. The SECM gold sample was characterized by CV in 0.1 M H₂SO₄ (Merck, Suprapur, 96%). The silver sample was characterized by thallium under potential deposition carried out in a mixture of 0.1 M Tl₂SO₄ (ACROS Organics, 99.9%, trace metal basis) + 0.1 M H₂SO₄ (Merck, Suprapur, 96%) + 0.5 M Na₂SO₄ (Alfa Aesar, Puratronic, 99.9955%, metals basis). The copper sample was characterized by CV in 0.1 M NaOH (Merck, EMPLURA, 32%). All the electrolytes were purged with argon prior to the characterization. For both the characterization and SECM measurements, a gold wire was used as the counter electrode when using the gold sample, and a platinum wire was used for the silver and copper electrodes. The Pt-UME was fabricated by etching and sealing a platinum wire (50 μm diameter, Goodfellow, 99.99%) into a soda lime glass capillary using a butane torch. The detailed procedure is reported elsewhere⁵⁰. The Pt-UME was polished before every set of SECM measurements and further cleaned by cycling 200 times between 0.06 and 1.60 V versus RHE in 0.1 M H₂SO₄ at 1 V s⁻¹, which always resulted in a reproducible blank voltammogram. The Pt-UME used in this work has a radius of approximately 6.5 ± 0.07 μm determined using the Fe(CN)₆³⁻/Fe(CN)₆⁴⁻ outer sphere reaction. Before the measurements, the tip-to-surface distance was determined using a capacitive approach performed in air. The details on the set-up can be found in our previous work³³. In short, using a function generator (33210A, Keysight), an a.c. voltage (10 kHz, 1.41 V (root mean square)) is applied to the sample to generate a capacitive current at the tip³³. This capacitive current was recorded as a function of distance using a virtual lock-in amplifier (LabView). Fitting this approach curve allowed us to determine the absolute tip-to-surface distance. Further details of the approach curve fitting can be found in the Supplementary Information. All SECM measurements were performed with the Pt-UME at a fixed distance (50 ± 2 μm) from the surface. A two-channel Bio-Logic potentiostat/galvanostat/EIS (SP-300) was used to control the sample and the tip individually. Chronoamperometry was performed at the sample for 10 s and subsequently the tip CV was recorded at 200 mV s⁻¹. During the experiments, the electrolyte was constantly purged with CO₂ or argon and an argon flow was kept above the solution to avoid oxygen diffusing into the solution. The electrolyte used was 1 mM H₂SO₄ (pH = 3) with the addition of 140 μM Cs₂SO₄ when necessary (Alfa Aesar, Puratronic, 99.997%, metals basis).

DFT parameters. DFT simulations were performed with the VASP code^{50,51}. We chose the Perdew–Burke–Ernzerhof density functional⁵², including dispersion through the DFT-D2 method^{53,54}, with our reparametrized C₆ coefficients⁵⁵. Inner electrons were represented by projector augmented wave pseudopotentials^{56,57} and the mono-electronic states for the valence electrons were expanded as plane waves with a kinetic energy cutoff of 450 eV.

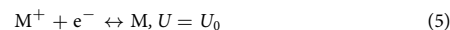
Computational model. Polycrystalline Au was modelled by a (3√3 × 3√3)R30° Au(111) (four layers, 15.3 Å × 15.3 Å × 30.0 Å, 8 Å vacuum thickness), which was geometrically optimized (two outermost layers relaxed, bulk fixed). The Brillouin zone was sampled at the Γ-point. As Pt and Au have similar lattice constants, we inherited the solvent configuration (72 H₂O molecules, 15 Å thick) optimized by AIMD for 11 ps at 300 K from our previous study regarding water–metal interface for (3√3 × 3√3)R30° Pt(111)³⁹. We inserted the pre-equilibrated water molecules on top of the Au surface and we carried out AIMD simulations for a total of 6 ps (1 ps of equilibration plus 5 ps production, with a 1 fs time step) in a canonical NVT (particle number, volume and temperature) ensemble at 300 K regulated by a Nosé–Hoover thermostat (Supplementary Methods)^{58–60}. First, we optimized

the hydrogen-bond network between the water molecules for 2 ps on the Au–H₂O system (Supplementary Fig. 8). Then, we inserted an alkali metal cation M⁺ (Li⁺, Na⁺, K⁺ or Cs⁺) in a cavity of the first solvation layer close to the surface as we removed a hydrogen from a water molecule in the fourth water bilayer to keep the charge balance. The cation coverage was set to 0.04 ML (1/27), which corresponded to a surface concentration of 0.5–0.8 M (Supplementary Methods). The resulting four systems were named Au–H₂O–M⁺ and underwent AIMD for an additional 2 ps. Finally, we added a CO₂ (0.04 ML, 1/27) to the Au–H₂O–M⁺ and four Au–H₂O–M⁺ proximal to the catalytic surface and the cation. The resulting four Au–H₂O–M⁺–CO₂ and one Au–H₂O–CO₂ systems underwent AIMD for 2 and 1 ps, respectively, and were used to investigate the activation of CO₂ in the presence and absence of an alkali cation (Supplementary Fig. 8). As the cation, CO₂ and the explicit water molecules were placed only on one side of the slab, we applied a dipole correction to remove spurious contributions that arose from the asymmetric slab model⁶¹.

Data analysis. Cation–water radial distribution functions were obtained for the 2 ps equilibration of the Au–H₂O–M systems, as described in Supplementary Methods. From these parameters, we determined the cation coordination number to water or CO₂ oxygens (Supplementary Methods). Finally, the CO₂ binding energy at U = 0.0 V versus SHE in the presence and absence of a cation was averaged from static DFT single-point calculations from AIMD configurations taken every 20 fs during the last 0.5 ps with the s.d. taken as uncertainty. Gibbs free energies were calculated from DFT energies by including entropic contributions at 298.15 K. The energy references were chosen as CO₂(g) and single-point calculations of the previously described Au–H₂O–CO₂ and Au–H₂O–M⁺–CO₂ configurations on removal of the CO₂ molecule (equation (4)), where the asterisk * represents a gold surface site).

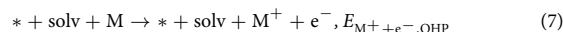


Cation accumulation at the OHP. To assess the thermodynamics of cation accumulation at the OHP, we applied the methodology introduced by Resasco et al.²⁷. The energy of a solvated cation at the bulk electrolyte can be referenced to the energy of the bulk alkali metal following the principles of the computational hydrogen electrode⁴⁴. At the standard reduction potential U₀ (ref. 62), a cation M⁺ is in equilibrium with its reduced state M (equation (5)). Thus, we can derive the energy of the cation/electron pair at a given potential U versus SHE from the DFT energy of the bulk alkali metal (equation (6)):



$$E_{M^+ + e^-} = E_M - |e^-| (U - U_0) \quad (6)$$

We can instead estimate the energy of a cation at the OHP at U = 0 V versus SHE from our AIMD simulations, as we specifically inserted an alkali metal at the OHP, which donates its valence electron to the solvation layer (equation (7)); the gold surface is represented by the symbol *, and the solvation layer is indicated by 'solv'. Thus, we can calculate the thermodynamic driving force for each cation to accumulate at the OHP as in equation (8). Considering the lowest energy configurations for Li⁺, Na⁺, K⁺ and Cs⁺ during the last 2 ps of the AIMD simulation, E_{OHP} – E_{bulk} (bulk electrolyte) correlates with the cation ionic radius⁶³. Cations with a larger radius are thermodynamically more prone to accumulate at the OHP, and thus they exhibit a higher concentration across the surface–electrolyte interface²⁷.



$$\Delta E = E_{M^+ + e^-, \text{OHP}} - E_{M^+ + e^-, \text{bulk}} \quad (8)$$

Data availability

The datasets generated through DFT simulation and analysed during the current study are available in the ioChem-BD database (ref. 64) at <https://doi.org/10.19061/iochem-bd-1-194> (ref. 65). Experimental datasets are available from the corresponding author upon reasonable request.

Received: 24 February 2021; Accepted: 17 June 2021;

Published online: 26 July 2021

References

- Kortlever, R., Shen, J., Schouten, K. J. P., Calle-Vallejo, F. & Koper, M. T. M. Catalysts and reaction pathways for the electrochemical reduction of carbon dioxide. *J. Phys. Chem. Lett.* **6**, 4073–4082 (2015).
- König, M., Vaes, J., Klemm, E. & Pant, D. Solvents and supporting electrolytes in the electrocatalytic reduction of CO₂. *iScience* **19**, 135–160 (2019).

- Moura de Salles Pupo, M. & Kortlever, R. Electrolyte effects on the electrochemical reduction of CO₂. *ChemPhysChem* **20**, 2926–2935 (2019).
- Setterfield-Price, B. M. & Dryfe, R. A. W. The influence of electrolyte identity upon the electro-reduction of CO₂. *J. Electroanal. Chem.* **730**, 48–58 (2014).
- Verma, S., Lu, X., Ma, S., Masel, R. I. & Kenis, P. J. A. The effect of electrolyte composition on the electroreduction of CO₂ to CO on Ag based gas diffusion electrodes. *Phys. Chem. Chem. Phys.* **18**, 7075–7084 (2016).
- Thorson, M. R., Siil, K. I. & Kenis, P. J. A. Effect of cations on the electrochemical conversion of CO₂ to CO. *J. Electrochem. Soc.* **160**, F69–F74 (2012).
- Banerjee, S., Zhang, Z., Hall, A. S. & Thoi, V. S. Surfactant perturbation of cation interactions at the electrode–electrolyte interface in carbon dioxide reduction. *ACS Catal.* **10**, 9907–9914 (2020).
- Zhang, Q., Shao, X., Yi, J., Liu, Y. & Zhang, J. An experimental study of electroreduction of CO₂ to HCOOH on SnO₂/C in presence of alkali metal cations (Li⁺, Na⁺, K⁺, Rb⁺ and Cs⁺) and anions (HCO₃⁻, Cl⁻, Br⁻ and I⁻). *Chinese J. Chem. Eng.* **28**, 2549–2554 (2020).
- Shen, J., Lan, D. & Yang, T. Influence of supporting electrolyte on the electrocatalysis of CO₂ reduction by cobalt protoporphyrin. *Int. J. Electrochem. Sci.* **13**, 9847–9857 (2018).
- Kyriacou, G. Z. & Anagnostopoulos, A. K. Influence of CO₂ partial pressure and the supporting electrolyte cation on the product distribution in CO₂ electroreduction. *J. Appl. Electrochem.* **23**, 483–486 (1993).
- Kim, H., Park, H. S., Hwang, Y. J. & Min, B. K. Surface-morphology-dependent electrolyte effects on gold-catalyzed electrochemical CO₂ reduction. *J. Phys. Chem. C* **121**, 22637–22643 (2017).
- Kim, H.-Y. et al. Analysis on the effect of operating conditions on electrochemical conversion of carbon dioxide to formic acid. *Int. J. Hydrog. Energy* **39**, 16506–16512 (2014).
- Gunathunge, C. M., Ovalle, V. J. & Waegle, M. M. Probing promoting effects of alkali cations on the reduction of CO at the aqueous electrolyte/copper interface. *Phys. Chem. Chem. Phys.* **19**, 30166–30172 (2017).
- Waegle, M. M., Gunathunge, C. M., Li, J. & Li, X. How cations affect the electric double layer and the rates and selectivity of electrocatalytic processes. *J. Chem. Phys.* **151**, 160902 (2019).
- Akhade, S. A., McCrum, I. T. & Janik, M. J. The impact of specifically adsorbed ions on the copper-catalyzed electroreduction of CO₂. *J. Electrochem. Soc.* **163**, F477–F484 (2016).
- Strmcnik, D. et al. Effects of Li⁺, K⁺, and Ba²⁺ cations on the ORR at model and high surface area Pt and Au surfaces in alkaline solutions. *J. Phys. Chem. Lett.* **2**, 2733–2736 (2011).
- Strmcnik, D. et al. The role of non-covalent interactions in electrocatalytic fuel-cell reactions on platinum. *Nat. Chem.* **1**, 466–472 (2009).
- Murata, A. & Hori, Y. Product selectivity affected by cationic species in electrochemical reduction of CO₂ and CO at a Cu electrode. *Bull. Chem. Soc. Jpn* **64**, 123–127 (1991).
- Hori, Y. & Suzuki, S. Electrolytic reduction of carbon dioxide at mercury electrode in aqueous solution. *Bull. Chem. Soc. Jpn* **55**, 660–665 (1982).
- Frumkin, A. N. Influence of cation adsorption on the kinetics of electrode processes. *Trans. Faraday Soc.* **55**, 156–167 (1959).
- Ringe, S. et al. Understanding cation effects in electrochemical CO₂ reduction. *Energy Environ. Sci.* **12**, 3001–3014 (2019).
- Chen, L. D., Urushihara, M., Chan, K. & Nørskov, J. K. Electric field effects in electrochemical CO₂ reduction. *ACS Catal.* **6**, 7133–7139 (2016).
- Hussain, G. et al. How cations determine the interfacial potential profile: relevance for the CO₂ reduction reaction. *Electrochim. Acta* **327**, 135055 (2019).
- Singh, M. R., Kwon, Y., Lum, Y., Ager, J. W. & Bell, A. T. Hydrolysis of electrolyte cations enhances the electrochemical reduction of CO₂ over Ag and Cu. *J. Am. Chem. Soc.* **138**, 13006–13012 (2016).
- Ayemoba, O. & Cuesta, A. Spectroscopic evidence of size-dependent buffering of interfacial pH by cation hydrolysis during CO₂ electroreduction. *ACS Appl. Mater. Interfaces* **9**, 27377–27382 (2017).
- Zhang, F. & Co, A. C. Direct evidence of local pH change and the role of alkali cation during CO₂ electroreduction in aqueous media. *Angew. Chem. Int. Ed.* **59**, 1674–1681 (2020).
- Resasco, J. et al. Promoter effects of alkali metal cations on the electrochemical reduction of carbon dioxide. *J. Am. Chem. Soc.* **139**, 11277–11287 (2017).
- Silvestrelli, P. L. Hydrogen bonding characterization in water and small molecules. *J. Chem. Phys.* **146**, 1–31 (2017).
- García, G. & Koper, M. T. M. Carbon monoxide oxidation on Pt single crystal electrodes: understanding the catalysis for low temperature fuel cells. *ChemPhysChem* **12**, 2064–2072 (2011).
- Jacobse, L., Raaijman, S. J. & Koper, M. T. M. The reactivity of platinum microelectrodes. *Phys. Chem. Chem. Phys.* **18**, 28451–28457 (2016).
- Bewick, A. & Thomas, B. Optical and electrochemical studies of the underpotential deposition of metals Part I. Thallium deposition on single crystal silver electrodes. *J. Electroanal. Chem.* **65**, 911–931 (1975).
- Schouten, K. J. P., Pérez-Gallent, E. & Koper, M. T. M. The electrochemical characterization of copper single-crystal electrodes in alkaline media. *J. Electroanal. Chem.* **699**, 6–9 (2013).
- Monteiro, M. C. O., Jacobse, L., Touzalin, T. & Koper, M. T. M. Mediator-free SECM for probing the diffusion layer pH with functionalized gold ultramicroelectrodes. *Anal. Chem.* **92**, 2237–2243 (2020).
- Voogd, J. M. De et al. Fast and reliable pre-approach for scanning probe microscopes based on tip-sample capacitance. *Ultramicroscopy* **181**, 61–69 (2017).
- Monteiro, M. C. O., Jacobse, L. & Koper, M. T. M. Understanding the voltammetry of bulk CO electrooxidation in neutral media through combined SECM measurements. *J. Phys. Chem. Lett.* **11**, 9708–9713 (2020).
- Henckel, D. A. et al. Potential dependence of the local pH in a CO₂ reduction electrolyzer. *ACS Catal.* **11**, 255–263 (2021).
- Lukaszewski, M., Soszko, M. & Czerwiński, A. Electrochemical methods of real surface area determination of noble metal electrodes—an overview. *Int. J. Electrochem. Sci.* **11**, 4442–4469 (2016).
- Macao, L. H., Santos, M. C., Machado, S. A. S. & Avaca, L. A. Underpotential deposition of silver on polycrystalline platinum studied by cyclic voltammetry and rotating ring-disc techniques. *J. Chem. Soc. Faraday Trans.* **93**, 3999–4003 (1997).
- Bellarosa, L., García-Muelas, R., Revilla-López, G. & López, N. Diversity at the water–metal interface: metal, water thickness, and confinement effects. *ACS Cent. Sci.* **2**, 109–116 (2016).
- Marcus, Y. Effect of ions on the structure of water: structure making and breaking. *Chem. Rev.* **109**, 1346–1370 (2009).
- Zhu, Q., Wallentine, S., Deng, G. & Baker, L. R. Solvation-induced Onsager reaction field rather than double layer field controls CO₂ reduction on gold. Preprint at <https://doi.org/10.26434/chemrxiv.14410655.v1> (2021).
- Birdja, Y. Y. et al. Advances and challenges in understanding the electrocatalytic conversion of carbon dioxide to fuels. *Nat. Energy* **4**, 732–745 (2019).
- Schizodimou, A. & Kyriacou, G. Acceleration of the reduction of carbon dioxide in the presence of multivalent cations. *Electrochim. Acta* **78**, 171–176 (2012).
- Nørskov, J. K. et al. Origin of the overpotential for oxygen reduction at a fuel-cell cathode. *J. Phys. Chem. B* **108**, 17886–17892 (2004).
- Peterson, A. A., Abild-Pedersen, F., Studt, F., Rossmeisl, J. & Nørskov, J. K. How copper catalyzes the electroreduction of carbon dioxide into hydrocarbon fuels. *Energy Environ. Sci.* **3**, 1311–1315 (2010).
- Rossmeisl, J., Chan, K., Ahmed, R., Tripković, V. & Björketun, M. E. pH in atomic scale simulations of electrochemical interfaces. *Phys. Chem. Chem. Phys.* **15**, 10321–10325 (2013).
- Bondue, C. J., Graf, M., Goyal, A. & Koper, M. T. M. Suppression of hydrogen evolution in acidic electrolytes by electrochemical CO₂ reduction. *J. Am. Chem. Soc.* **143**, 279–285 (2021).
- Monteiro, M. C. O. & Koper, M. T. M. Alumina contamination through polishing and its effect on hydrogen evolution on gold electrodes. *Electrochim. Acta* **325**, 134915 (2019).
- Do, U. P., Seland, F. & Johannessen, E. A. The real area of nanoporous catalytic surfaces of gold and palladium in aqueous solutions. *J. Electrochem. Soc.* **165**, H219–H228 (2018).
- Kresse, G. & Furthmüller, J. Efficient iterative schemes for ab initio total-energy calculations using a plane-wave basis set. *Phys. Rev. B* **54**, 11169–11186 (1996).
- Kresse, G. & Furthmüller, J. Efficiency of ab-initio total energy calculations for metals and semiconductors using a plane-wave basis set. *Comput. Mater. Sci.* **6**, 15–50 (1996).
- Perdew, J. P., Burke, K. & Ernzerhof, M. Generalized gradient approximation made simple. *Phys. Rev. Lett.* **77**, 3865–3868 (1996).
- Grimme, S. Semiempirical GGA-type density functional constructed with a long-range dispersion correction. *J. Comput. Chem.* **27**, 1787–1799 (2006).
- Bucko, T., Hafner, J., Lebègue, S. & Ángyán, J. G. Improved description of the structure of molecular and layered crystals: ab initio DFT calculations with van der Waals corrections. *J. Phys. Chem. A* **114**, 11814–11824 (2010).
- Almora-Barrios, N., Carchini, G., Błoński, P. & López, N. Costless derivation of dispersion coefficients for metal surfaces. *J. Chem. Theory Comput.* **10**, 5002–5009 (2014).
- Blöchl, P. E. Projector augmented-wave method. *Phys. Rev. B* **50**, 17953–17979 (1994).
- Kresse, G. & Joubert, D. From ultrasoft pseudopotentials to the projector augmented-wave method. *Phys. Rev. B* **59**, 1758–1775 (1999).
- Marx, D. & Hutter, J. *Ab Initio Molecular Dynamics: Basic Theory and Advanced Methods* (Cambridge Univ. Press, 2009).
- Nosé, S. A unified formulation of the constant temperature molecular dynamics methods. *J. Chem. Phys.* **81**, 511–519 (1984).
- Hoover, W. G. Canonical dynamics: equilibrium phase-space distributions. *Phys. Rev. A* **31**, 1695–1697 (1985).

61. Makov, G. & Payne, M. Periodic boundary conditions in ab initio calculations. *Phys. Rev. B* **51**, 4014–4022 (1995).
62. Haynes, W. M. *Handbook of Chemistry and Physics* (CRC, 2014).
63. Lide, D. R. *CRC Handbook of Chemistry and Physics* Vol. 85 (CRC, 2003).
64. Álvarez-Moreno, M. et al. Managing the computational chemistry big data problem: the ioChem-BD platform. *J. Chem. Inf. Model.* **55**, 95–103 (2015).
65. Dattila, F. Cation effect CO₂ reduction. *ioChem-BD* <https://doi.org/10.19061/iochem-bd-1-194> (2021).

Acknowledgements

This work was supported by the European Commission (Innovative Training Network ELCOREL, 722614-ELCOREL). F.D., R.G.-M. and N.L. further acknowledge the Barcelona Supercomputing Center (BSC-RES) for providing generous computational resources.

Author contributions

M.C.O.M. and F.D. wrote the manuscript with input from all the authors. M.C.O.M. and M.T.M.K. designed the experiments, which were carried out by M.C.O.M. with assistance

from B.H., F.D. R.G.-M. and N.L. carried out the DFT AIMD simulations. All the authors contributed to the modelling section, read and commented on the manuscript.

Competing interests

The authors declare no competing interests.

Additional information

Supplementary information The online version contains supplementary material available at <https://doi.org/10.1038/s41929-021-00655-5>.

Correspondence and requests for materials should be addressed to M.T.M.K.

Peer review information *Nature Catalysis* thanks Leanne Chen and the other, anonymous, reviewer(s) for their contribution to the peer review of this work.

Reprints and permissions information is available at www.nature.com/reprints.

Publisher's note Springer Nature remains neutral with regard to jurisdictional claims in published maps and institutional affiliations.

© The Author(s), under exclusive licence to Springer Nature Limited 2021